

Curvature-driven adsorption of cationic nanoparticles to phase boundaries in multicomponent lipid bilayers: Supporting information

Jonathan K. Sheavly¹, Joel A. Pedersen², and Reid C. Van Lehn¹

¹Department of Chemical and Biological Engineering, University of Wisconsin-Madison, 1415 Engineering Drive, Madison, WI, USA. E-mail: vanlehn@wisc.edu

²Departments of Soil Science, Chemistry, and Civil & Environmental Engineering, University of Wisconsin-Madison, 1525 Observatory Drive, Madison, WI, USA.

Section S1 Comparison of coarse-grained water models

All simulations discussed in the main text were performed using the big multipole water (BMW) coarse-grained water model,¹ which was developed to be used with the MARTINI force field. We chose the BMW model because it more accurately reproduces the membrane potential measured by atomistic simulations than either the standard MARTINI water model or the more recent polarizable MARTINI water model,² as we reasoned that the membrane potential could affect NP-bilayer interactions dramatically. To confirm this behavior, we measured the electrostatic potential using the GROMACS tool *gmx potential* for the one-phase L_d bilayer using each of the coarse-grained water models. As recommended, the system-wide dielectric constant was set to 2.5 for the polarizable MARTINI water model,² 15 for the standard MARTINI water model,³ and 1.3 for the BMW model.¹ The electrostatic potential was also measured for a single-component DOPC bilayer modeled using the all-atom CHARMM36 force field with the SPC/E water model and matches previous simulation results.⁴ Figure S1a shows that both the standard MARTINI water model (W) and the polarizable water model (PW) predict the wrong sign for the membrane potential when compared to the atomistic results, while the BMW water model correctly captures the sign of the potential and features near the bilayer-water interface.

To further justify the selection of the BMW water model, Figure S1b compares potentials of mean force (PMFs) for NP adsorption to the one-phase L_d bilayer using the polarizable and standard MARTINI water models; these PMFs can be compared to the PMFs reported in Figure 2 of the main text. Figure S1b shows that the PMF for the polarizable MARTINI water model is purely repulsive, which contradicts experimental measurements indicating favorable adsorption of cationic NPs to one-phase L_d bilayers.⁵ We thus reject this water model as a reasonable possibility. Figure S1b shows that the PMF for the standard water model exhibits minimal interaction until the NP effectively comes into contact with the bilayer, at which point there is a weak free energy minimum. We again reject this model due to the weak adsorption free energy and incorrect membrane potential. Finally, we note that the improvement with BMW does not necessarily imply that the electrostatic interactions drive adsorption to the charge-neutral lipid bilayers studied in this work, but rather could indicate that other water models introduce spurious electrostatic interactions that lead to inaccurate adsorption free energies for cationic NPs.

Section S2 Additional simulation parameters

The BMW forcefield uses a modified Born-Mayer-Huggins potential⁶ with a smooth switching function between 1.0 nm and 1.4 nm to model interactions with water. This potential is not included as a standard functional form in GROMACS,¹ so forces are explicitly tabulated for solvent-solvent, solvent-nonsolvent and nonsolvent-nonsolvent interactions as provided by the creators of the model.¹ Electrostatic interactions are modeled using the smooth Particle Mesh Ewald method with a 1.4 nm short-range cutoff, 0.2 nm grid spacing, and sixth-order interpolation. Additionally, a system-wide relative dielectric constant of 1.3 is applied as suggested.¹ Verlet lists were generated

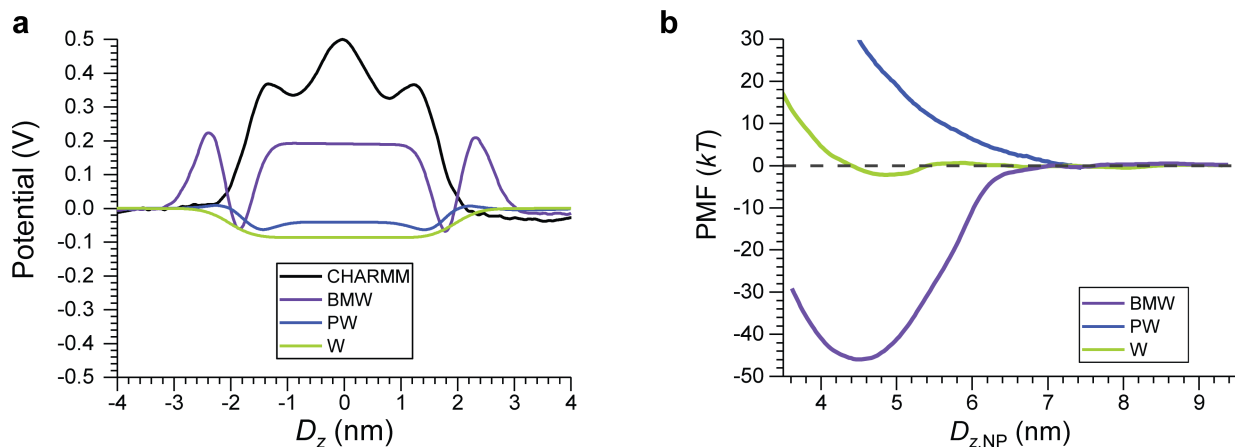


Figure S1: **a)** Electrostatic potential near a L_d bilayer computed using the polarizable MARTINI water model (PW), the standard MARTINI water model (W), the big multipole water model (BMW), and an atomistic reference (CHARMM). D_z measures the z -component of the distance to the center-of-mass of the bilayer. **b)** Potential of mean force (PMF) for NP adsorption to a one-phase L_d bilayer using each coarse-grained water model as a function of the z -component of the distance between the NP and the center-of-mass of the bilayer ($D_{z, NP}$).

using a 1.4 nm cutoff. All molecular dynamics simulations were performed using a leapfrog integrator with a 20 fs timestep.

In order to adapt the MARTINI model to the BMW water model parameters, the original creators of the BMW model recommend a different CG bead for counterions and a special cationic bead to differentiate between the guanidinium group (present in arginine) and the amino group (present in lysine).^{1,7} Both recommendations were followed in this work. These changes modify the interactions between these species and the BMW water molecule, which is parameterized to reproduce experimental binding effects.⁷

Section S3 Description of bilayer components

Phase-separated lipid bilayers have been previously modeled using the MARTINI force field as a ternary mixture of the unsaturated lipid DIPC, the saturated lipid DPPC, and cholesterol.⁸ Figure S2 shows chemical structures for these molecules while their simulation representations are shown in Fig. 1 of the main text. DIPC is a doubly unsaturated lipid, which is not representative of typical lipids contained within model membranes - for example, the singly unsaturated lipid DOPC is more commonly used in raft-like membranes experimentally.^{5,9} However, our focus is not on modeling phase separation precisely, but rather to determine how the properties of various lipid phases affect nanoparticle (NP) interactions. We thus use DIPC as a model lipid to obtain phase separation because it has previously been shown to phase separate at room temperature in other MARTINI simulations.¹⁰

Section S4 Preparation of one-phase bilayers

Both one-phase bilayers were initially prepared in a $14 \times 14 \times 24$ nm³ simulation box using the INSANE script,¹¹ which was also used to insert the NP into the system with an initial value of $D_{z, NP} = 8$ nm. The INSANE script was modified to prevent water molecules from being added to the middle of the hollow NP core. Both systems were also prepared using the same protocol but without the NP for simulations that were used to calculate bilayer structural properties. Table S1 summarizes the components of each system, including the neutralizing counterions.

Equilibration simulations for all one-phase bilayer systems were performed using the following protocol. The systems were first simulated for 10 ns at constant volume and with the temperature maintained at $T = 295$ K using a Berendsen thermostat with a 1 ps coupling constant. The systems were then simulated for an additional 20 ns with the pressure maintained at 1 bar using a semi-isotropic Berendsen barostat with a 2.0 ps coupling constant and

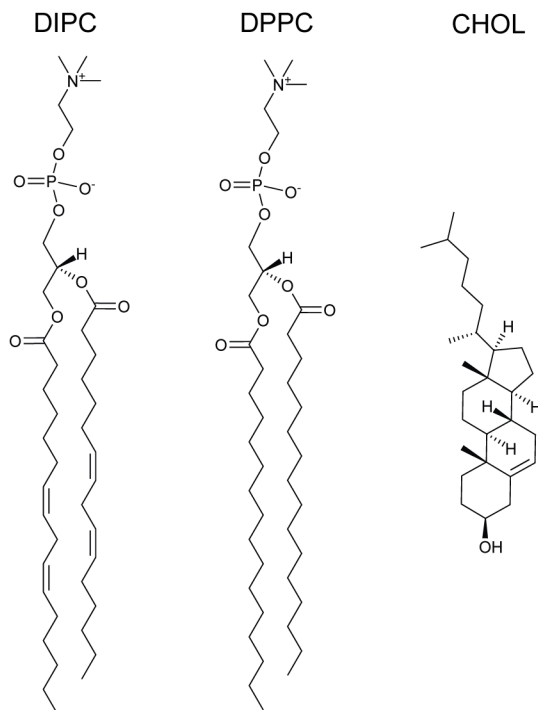


Figure S2: Chemical structures of bilayer components.

Table S1: Number of molecules in each simulation system

Species	One-phase L_o	One-phase L_d	Two-phase
DIPC	-	648	684
DPPC	324	-	494
CHOL	324	-	494
Water	20,303	31,669	53,079
Chloride	240	240	240

$3 \times 10^{-5} \text{ bar}^{-1}$ compressibility.¹ These parameters follow prior MARTINI examples.^{1,10,12} No restraint was placed on the NP during these simulations. The equilibrium box dimensions for the L_d bilayer were $14.70 \times 14.70 \times 20.75 \text{ nm}^3$ and the dimensions for the L_o bilayer were $11.21 \times 11.21 \times 23.43 \text{ nm}^3$ after the constant pressure equilibration. The final configurations after equilibration were used to initialize umbrella sampling as described in Section S6.

To confirm that the simulation box dimensions are reasonable, Figure S3 shows the average bilayer height for the L_d bilayer as a function of the radial distance from an adsorbed NP ($D_{r, \text{NP}}$). The bilayer height was defined for each lipid as the difference between the position of the PO4 bead and the bilayer midplane, projected along the z -axis. Each point in Figure S3 corresponds to the bilayer height averaged over all lipids within a thin radial shell with a thickness of 0.5 nm, computed from a 100 ns constant pressure simulation in a $20 \times 20 \times 14 \text{ nm}^3$ simulation box (a larger system size than eventually selected) performed after the equilibration protocol described above. The height decays to a constant value of 1.93 nm at a radial distance 5.0 nm from the center of mass of the NP, indicating that a minimum box dimension of 10.0 nm is necessary to ensure that bilayer perturbations decay prior to the periodic boundaries. This value is smaller than the final equilibrated dimensions of the bilayers used to generate the results in the main text, indicating that the chosen system size is sufficient.

We further compared the structural properties of the bilayers to previously published values by computing the area per lipid and bilayer thickness. The area per lipid was approximated as the total area of the $x - y$ plane of the simulation box divided by the number of lipids in a single leaflet. The bilayer thickness was computed by

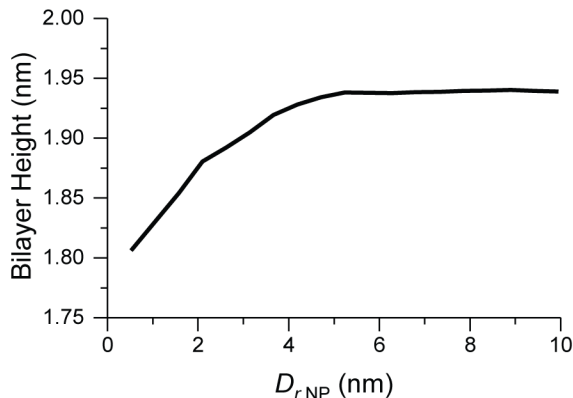


Figure S3: The average bilayer height as a function of the radial distance from an adsorbed NP ($D_{r,NP}$) for an enlarged L_d bilayer. The bilayer height plateaus by $D_{r,NP}=5.0$ nm.

subtracting the average z -position of the phosphate groups in the bottom leaflet from the average z -position of the phosphate groups in the top leaflet. The area per lipid and thickness of each one-phase bilayer were computed from 100 ns trajectories performed in the absence of a NP. The results of these structural measurements (Table S2) are in good agreement with prior MARTINI simulations,⁸ atomistic simulations,¹³ and experimental measurements.¹⁴ These measurements confirm that simulations with the BMW model yield reasonable bilayer structural properties.

Table S2: Comparison of one-phase bilayer structural parameters

	This work		Experiments ¹⁴	
	L_o	L_d	L_o	L_d
Bilayer thickness (nm)	4.54	3.83	4.42	3.59
Area per lipid (nm ²)	0.775	0.667	0.71	0.652

Section S5 Preparation of two-phase bilayer

The two-phase bilayer was initially prepared in a $15 \times 34 \times 17$ nm³ simulation box by merging non-equilibrated L_o and L_d bilayers generated with the INSANE script. The NP was introduced 5 nm above the L_o phase using the modified INSANE script. The bilayer was also prepared using the same protocol but without the NP to calculate properties of the phase-separated bilayer. Table S1 summarizes the components of the two-phase bilayer system, including neutralizing counterions.

The two-phase bilayer system was first simulated for 10 ns at constant volume and with the temperature maintained at $T = 295$ K using a Berendsen thermostat with a 1 ps coupling constant. The system was then simulated for an additional 10 ns with the pressure maintained at 1 bar using an anisotropic Berendsen barostat with a 2.0 ps coupling constant and 3×10^{-5} bar⁻¹ compressibility.¹ No restraint was placed on the NP during these simulations. The equilibrium box dimensions for the two-phase bilayer system were $14.27 \times 28.9 \times 18.5$ nm³ after the constant pressure equilibration. The final configuration after equilibration was used to initialize the umbrella sampling protocol described below.

To confirm that the simulation box dimensions are reasonable, Figure S4a shows the average height of the two-phase bilayer as a function of the distance from the COM of the L_o phase projected onto the y -axis (D_y). Height profiles were computed from a 100 ns constant pressure simulation for bilayers with varying initial y -dimensions (note that the phase boundary is perpendicular to the y -axis). For all box dimensions, the bilayer height smoothly interpolates between a smaller value in the L_d phase to a larger value in the L_o phase. The width of the phase boundary, or the region where the height changes, depends on the size of the box, as does the thickness of the

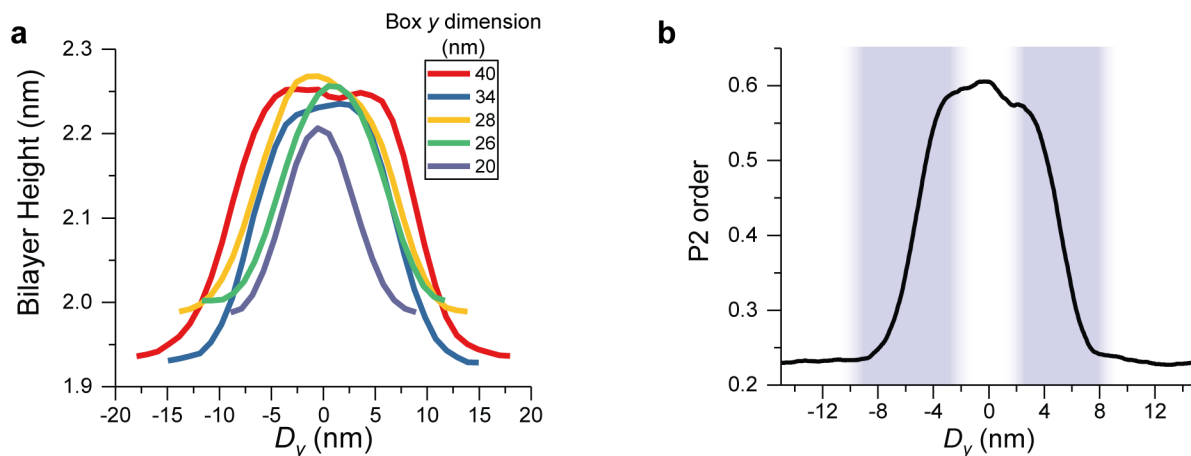


Figure S4: Effect of system size on two-phase bilayer properties in the absence of a NP. **a)** Average bilayer height as a function of D_y for a two-phase bilayer. Each curve reports the height for a different initial simulation box y -dimension prior to equilibration. Distinct plateaus in regions corresponding to the L_d and L_o phases are only observed for the 34 and 40 nm box sizes. **b)** P_2 order parameter as a function of D_y for a two-phase bilayer. The initial box y -dimension prior to equilibration was 34 nm, the same value used in the main text. The two phase boundaries are shaded in blue.

L_d phase. We find that the height plateaus to a characteristic value in each phase for the 34 nm box and obtains similar values to those reported for the one-phase bilayers. While the 40 nm box leads to a further increase in the width of the boundary, we chose to use an initial y -dimension of 34 nm (as noted above) because two phases are clearly obtained and further increasing the size to 40 nm would require a significant increase in computational expense (both due to a larger system size and an increased number of windows necessary for umbrella sampling). With this system size, we expect the width of the L_o phase to be relatively small (approximately 4 nm as shown in Figure S4) but large enough to replicate the behavior of the bulk L_o phase.

We further computed the P_2 order parameter to distinguish between the L_d phase and L_o phase in the two-phase bilayer. The P_2 order parameter is defined as:

$$P_2 = \frac{1}{2}(3\cos^2\theta - 1) \quad (1)$$

where θ is the angle between the membrane normal (taken as the z -axis) and the vector between two bonded lipid tail beads. The value of P_2 was averaged over all pairs of bonded lipid tail beads and over all configurations; a value near one indicates that the lipid tails are aligned with the membrane normal. Figure S4b shows the P_2 order parameter computed from a 100 ns constant pressure simulation performed using an initial y -dimension of 34 nm (equivalent to the value used in the main text). As expected, the parameter smoothly varies from a low value in the L_d phase, indicating disordered lipid tails, to a higher value in the L_o phase, indicating ordered lipid tails. Values plateau in both phases indicating well-converged simulations with a sufficient box size. We define the region where the P_2 order parameter plateaus at approximately 0.22 as the L_d phase and the region where the P_2 order parameter plateaus at approximately 0.61 as the L_o phase, with the remainder of the system defined as the phase boundary. For comparison, we also computed the P_2 order parameter for the one-phase L_d bilayer, the one-phase L_o bilayer, and a one-phase L_d bilayer containing 10% cholesterol (CHOL; further discussed in Section S12 below). These values are reported in Table S3 and are identical to the plateau values obtained for the two-phase bilayer. Finally, we also used the P_2 order parameter to estimate the curvature modulus, K_c , as a function of D_y :

$$K_c(D_y) = K_{c,L_d} + (K_{c,L_o} - K_{c,L_d}) \frac{(P_2(D_y) - P_{2,L_d})}{(P_{2,L_o} - P_{2,L_d})} \quad (2)$$

where K_{c,L_o} and K_{c,L_d} are the curvature moduli for the pure phases and P_{2,L_d} and P_{2,L_o} are the P_2 order parameters at the two plateau regions.

Section S6 Details on umbrella sampling methods

For each one-phase system, initial configurations for umbrella sampling were generated by applying an umbrella potential with a spring constant of 6000 J/mol/nm² to pull the NP along the z -axis toward the bilayer surface at a rate of 0.0001 nm/ps for 60 ns. 60 configurations spaced by 0.1 nm along the z -axis were then extracted from this trajectory. Umbrella sampling was initiated from each configuration and performed for 155 ns using a spring constant of 6,000 J/mol/nm² to obtain well-centered, overlapping histograms. The first 55 ns of each trajectory were discarded as equilibration and the PMF was obtained from the remaining 100 ns using the Weighted Histogram Analysis Method as implemented in the program *gmx wham*.¹⁵

To evaluate PMF convergence for the one-phase systems, we calculated the PMF minimum as a function of the amount of sampling time included in the WHAM calculation. We performed this analysis for the one-phase L_d, L_o, and the L_d bilayer with 10% cholesterol (described in Section S12 below). Figure S6a shows the minimum value of the PMF as a function of sampling time after the initial 55 ns of equilibration. For each point, a separate WHAM calculation was performed to obtain the PMF using the indicated amount of sampling time, the PMF was shifted such that its average value for the largest 0.2 nm of the reaction coordinate was zero, and the PMF minimum was determined. The plot shows that the PMF minimum in each system plateaus by 50 ns of sampling time, indicating that 50 ns of sampling is sufficient to obtain a converged PMF. Based on this data, Figure 2 in the main text reports the average and standard deviation from two independent calculations of the PMF performed using separate 50 ns intervals, each again shifted such that the average value for the largest 0.2 nm of the reaction coordinate was zero. The average PMF minimum computed from these two separate calculations is reported as a dashed line for each one-phase bilayer in Figure S6a.

For the two-phase system, initial configurations for umbrella sampling were generated by first applying an umbrella potential with a spring constant of 6,000 J/mol/nm² to pull the NP along the z -axis the NP toward the bilayer surface at a rate of 0.0001 nm/ps for 50 ns until $D_{z, \text{NP}} = 5.5$ nm, then applying another umbrella potential with a spring constant of 4,000 J/mol/nm² to pull the NP along the y -axis orthogonal to the phase boundary at a rate of 0.0001 nm/ps for 144 ns. All lipid head groups were restrained during this initial pulling process to prevent the displacement of lipids due to the rapid motion of the NP across the phase boundary. 144 configurations spaced by 0.1 nm along the y -axis were then extracted from this trajectory, including configurations where the NP is above the L_o phase, the L_d phase, and the phase boundary. Umbrella sampling was then performed for 250 ns per window using a spring constant of 6,000 J/mol/nm² to obtain well-centered, overlapping histograms. An anisotropic barostat was used with the compressibility in the y -direction set to zero to prevent the box from being resized along the reaction coordinate. The direction-periodic geometry, implemented in GROMACS, was used to define the distance between the COM of the NP and the COM of the L_o phase ($D_{y, \text{NP}}$) as the reaction coordinate to avoid artifacts associated with periodic boundary conditions. We defined the COM of the L_o phase as the COM of all DPPC lipids because no DPPC lipids were observed in the L_d phase of the two-phase bilayer, as shown in Figure 5a of the main text and further discussed in Section S8 below. An atom in the center of the L_o phase was used as a reference for distance calculations to ensure consistent calculation of the COM. The first 100 ns of each trajectory were discarded as equilibration and the PMF was obtained from the remaining 150 ns using WHAM.

To evaluate PMF convergence for the two-phase system, Figure S5b shows the difference between the minimum and maximum value of the PMF and the difference between the value of the PMF in the L_d phase and the value of the PMF in the L_o phase as a function of sampling time. For this calculation, the value of the PMF in the L_d phase was defined as the average value of the PMF in the range $-14.0 \leq D_{y, \text{NP}} \leq -13.8$ nm and the value of the PMF in the L_o phase was defined as the average value of the PMF in the range $-0.2 \leq D_{y, \text{NP}} \leq 0.0$ nm. The plot shows that both metrics plateau within 75 ns, indicating that 75 ns of sampling is sufficient to obtain a converged PMF. Based on this data, Figure 5b in the main text reports the average and standard deviation from two independent calculations of the PMF performed using separate 75 ns intervals, each shifted such that the average value of the PMF in the range $-14.0 \leq D_{y, \text{NP}} \leq -13.8$ nm was zero. The average minimum value of the PMF computed from these two separate PMFs is reported as a dashed line for each metric in Figure S6b.

Table S3: Comparison of one-phase bilayer order parameters

	L _d	L _o	L _d with 10% CHOL
P_2 order parameter	0.22	0.61	0.23

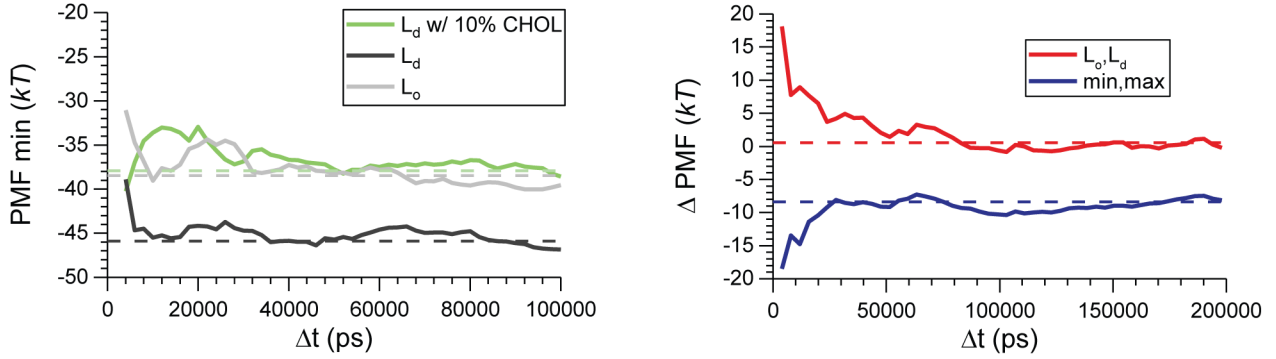


Figure S5: **a)** PMF convergence for the one-phase L_o, L_d, and L_d with 10% CHOL bilayers. Each line indicates the PMF minimum as a function of sampling time. The dashed lines indicate the average PMF minima computed using separate 50-ns blocks as reported in the main text. **b)** PMF convergence for the two-phase bilayer. The red line indicates the difference in the value of the PMF between the L_d phase and the L_o phase while the blue line indicates the difference in the PMF minimum and maximum. The dashed lines indicate the average values of these quantities computed using separate 75-ns blocks as reported in the main text.

Section S7 Robustness of one-phase umbrella sampling parameters

To further confirm the robustness of the simulation results for the one-phase bilayers, we performed several additional umbrella sampling simulations to determine the effect of changes to simulation parameters on the resulting PMFs. First, we performed umbrella sampling using the “cylinder” geometry, as implemented in GROMACS 2016, to compute the reaction coordinate and obtained corresponding PMFs for adsorbing a NP to one-phase L_d and L_o bilayers. Using the cylinder geometry requires the radius of the cylinder, r_{cyl} , to be selected as a tuning parameter. Only lipids within this radial distance from the NP COM (computed in the $x - y$ plane of the simulation box) are used to compute the z -component of the distance between the NP COM and the lipid COM of mass (*i.e.*, the reaction coordinate). Moreover, each lipid’s contribution to the reaction coordinate is computed using a weight function to avoid large jumps in the pull force associated with lipid diffusion into/out of the cylinder. This weight function is defined as:

$$\begin{aligned}
 w(r < r_{cyl}) &= 1 - 2 \left(\frac{r}{r_{cyl}} \right)^2 + \left(\frac{r}{r_{cyl}} \right)^4 \\
 w(r \geq r_{cyl}) &= 0
 \end{aligned}
 \tag{3}$$

where w is the weight for a single lipid a distance r from the NP COM (computed in the $x - y$ plane of the simulation box). The weight function thus smoothly transitions between a value of one directly underneath the NP and zero at the edge of the cylinder, such that lipids directly beneath the projected area of the NP contribute most significantly to the calculation of the reaction coordinate. However, this definition of the reaction coordinate can lead to radial forces if r_{cyl} is too small. We chose $r_{cyl} = 6$ nm; we found that any smaller radius led to numerical stability issues, potentially due to the presence of these radial forces. 60 initial configurations were re-generated using the cylinder geometry and umbrella sampling was performed following the protocol described in Section S6.

We also studied the role of the pulling direction used to generate initial configurations for umbrella sampling by pulling an initially adsorbed NP away from the bilayer. However, during this pulling trajectory the bilayer deformed significantly (with much larger out of plane deformations than observed when pulling the NP toward the bilayer) as shown in Figure S6a. We believe that these deformations are spurious and resulted from being unable to pull the NP infinitely slowly. We instead attempted to remove any bias associated with pulling direction by restraining the positions of all lipids while pulling the NP away from the bilayer to the desired distance, then removing these restraints to allow the bilayer to deform in response to the NP during the following equilibration and umbrella sampling simulations. Figure S6a compares bilayer height profiles between configurations generated

using this approach, which leads to bilayer heights that are similar to those shown in Figure 4b of the main text. 60 new initial configurations were generated from this pulling trajectory and used to perform umbrella sampling following the protocol described in Section S6.

Finally, we also tested the effect of changing the barostat used during umbrella sampling. We performed umbrella sampling using the same protocol described in Section S6 but using a semi-isotropic Parrinello-Rahman (PR) barostat and Nose-Hoover thermostat. The barostat time constant was 6.0 ps, the reference pressure was 1.0 bar, and the compressibility was $3 \times 10^{-5} \text{ bar}^{-1}$, while the thermostat time constant was 1 ps and the reference temperature was 295 K.

Figure S6 summarizes the results of these robustness checks. All simulations were performed for 155 ns per simulation window with the first 55 ns discarded as convergence to replicate the approach used for the simulations reported in the main text (discussed in Section S6). Figure S6b reports the convergence of the four additional PMFs (two using the cylinder geometry, one using a different pulling direction when generating initial conditions, and one using the PR barostat) based on the PMF minima following the procedure described in Section S6. Figure S6c compares the PMF minima obtained for each of the four additional PMFs to the PMF minima obtained for the three one-phase bilayers computed using the protocol in Section S6 and Figure S6d reports the values of the reaction coordinates that correspond to these minima. These results show that there are only small changes in the reported PMF minima between all of the various robustness checks that are largely within the reported error. Notably, changing the method for generating initial configurations results in negligible change in the PMF minimum. Using the cylinder geometry does decrease the magnitude of the PMF minimum, but a similar decrease is observed for both the L_d and L_o bilayers. There are slight downward trends in Figure S6B that indicate that the PMFs for the robustness checks may not be fully converged, but the differences are small relative to the magnitude and differences between the PMF minima. These data thus indicate that only small changes to the PMF values are observed when changing simulation parameters, and critically no significant change in the relative values computed for different bilayer phases is observed, thus demonstrating the robustness and reproducibility of the results presented in the main text.

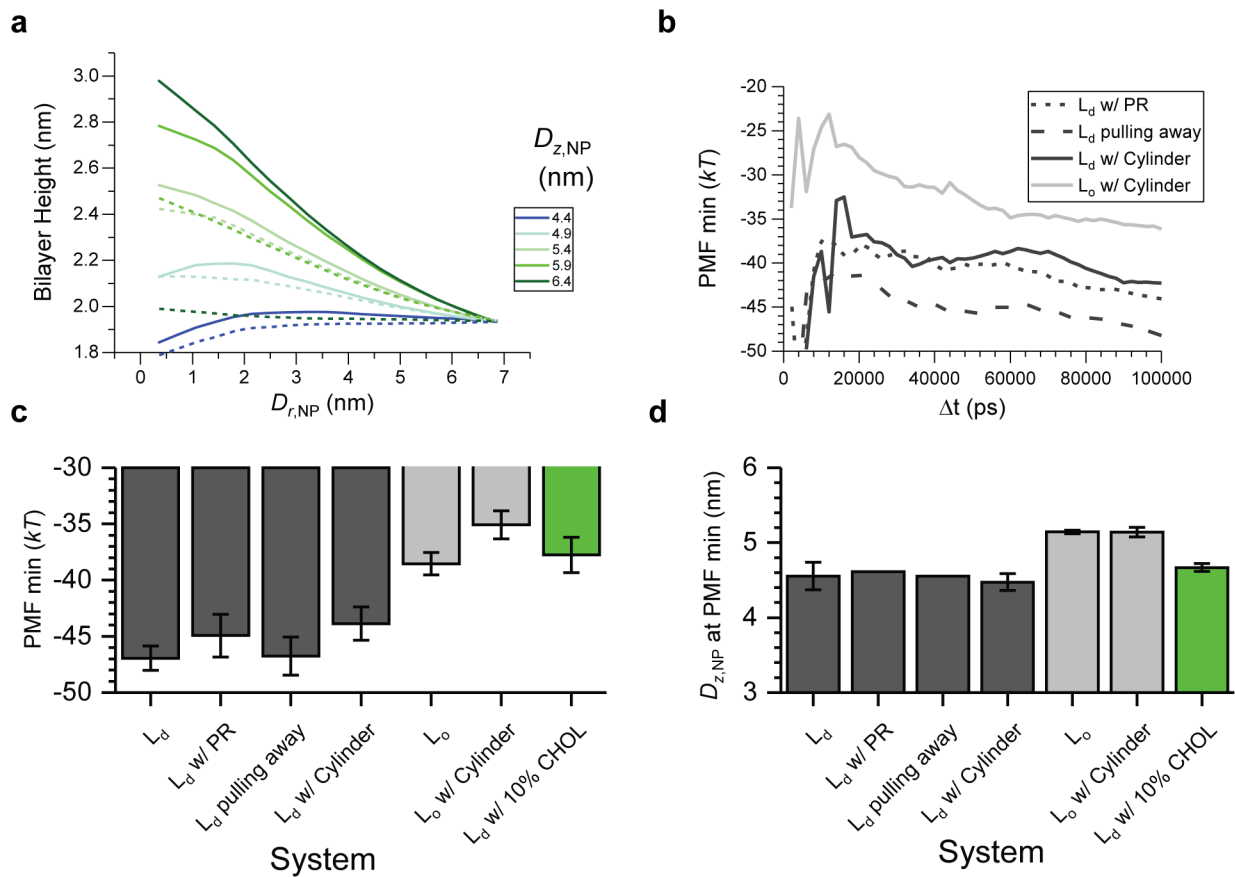


Figure S6: **a)** Bilayer height as a function of $D_{r,NP}$ for a one-phase L_d bilayer for various values of $D_{z,NP}$, computed from simulations in which the NP was slowly pulled away from the bilayer while keeping the lipid positions restrained (dashed) or unrestrained (solid). **b)** PMF convergence for each robustness check. Each line plots the PMF minimum as a function of sampling time. **c)** PMF minima computed for all robustness checks and the results presented in the main text. **d)** Values of $D_{z,NP}$ corresponding to the PMF minima presented in **c)**.

Section S8 Stability of two-phase boundary and phase compositions

We performed multiple tests to confirm that the reaction coordinate chosen for the two-phase system, $D_{y, \text{NP}}$, is reasonable. A possible error that could arise for the two-phase system is variations in the PMF due to fluctuations of the phase boundary in the x -direction orthogonal to the reaction coordinate in the presence of an adsorbed NP. To show that fluctuations of the phase boundary are small, Figure S7a shows color maps illustrating the height of the two-phase bilayer as a function of position in the $x - y$ plane in the absence of a NP and with an adsorbed NP positioned at various values of $D_{y, \text{NP}}$. The height is calculated following the method described in Section S10. In the absence of the NP, the height of the bilayer is nearly constant in the regions corresponding to the two individual phases and a well-defined vertical (*i.e.*, parallel to the x -axis) phase boundary is observed, agreeing with Figure 5a of the main text. Similar features are observed even in the presence of the adsorbed NP. Most importantly, the phase boundary is still vertical for all four representative NP positions, indicating that the position is not significantly affected by the presence of the NP and fluctuations of the phase boundary in the y -direction are not significant.

Another error that could arise from the definition of $D_{y, \text{NP}}$ as the distance between the NP and the COM of DPPC lipids is changes in the value of the reaction coordinate due to the diffusion of DPPC lipids into the L_d phase. Since the prior discussion indicates that the y -position of the phase boundary is stable in the presence of the NP and the phase boundary undergoes minimal fluctuations, we quantified lipid interdiffusion by measuring the standard deviation in the composition of the system as a function of the reaction coordinate, following a similar procedure as in Figure 5a of the main text. We time-averaged the bilayer composition (defined as the mole fraction of each component) using all configurations for which the PMF was measured (*i.e.*, 150 ns of sampling for each of the 144 windows). The resulting standard deviation in composition is plotted as error bars in Figure S7b. This plot shows that the amount of DPPC in the L_d phase remains nearly zero during umbrella sampling, indicating that minimal diffusion of DPPC lipids into the L_d phase is observed. The relatively small fluctuations for all species reinforces the conclusion that the phase boundary position and shape do not fluctuate significantly during umbrella sampling and that the definition of the reaction coordinate is robust with respect to these possible errors.

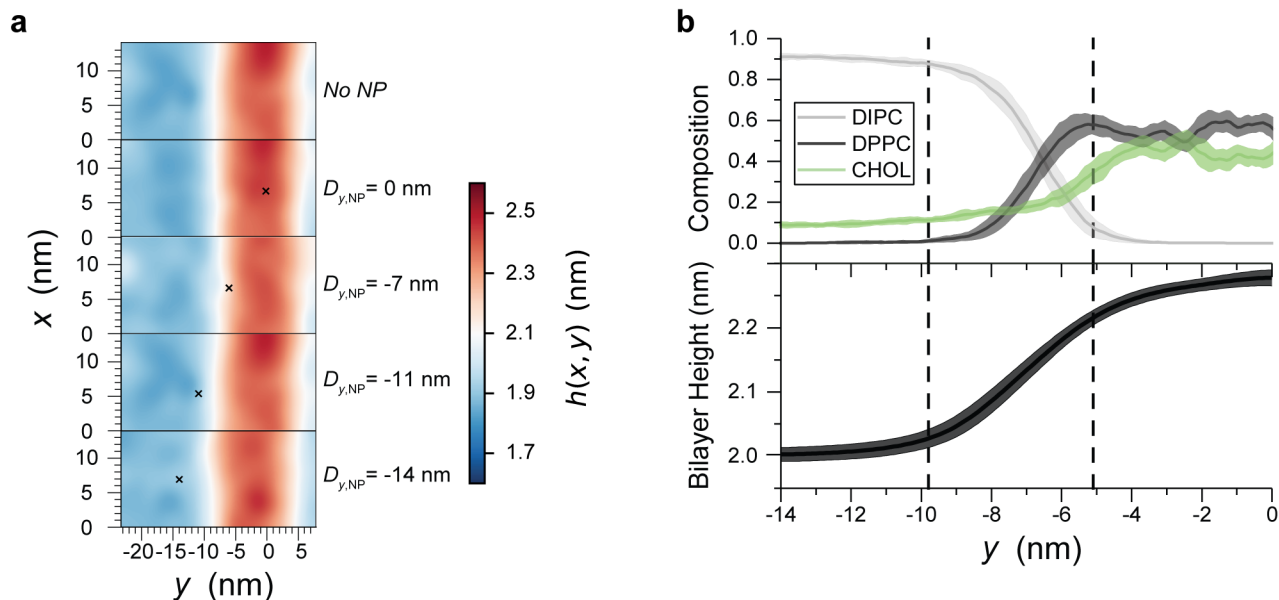


Figure S7: **a)** Bilayer height computed from umbrella sampling simulations for a two-phase bilayer at various values of $D_{y, \text{NP}}$. The X in the color maps indicates the average position of the NP COM. The top color map indicates a bilayer without an adsorbed NP. **b)** Bilayer height and composition for a two-phase bilayer as a function of D_y computed using all umbrella sampling trajectories. The line represents the average across all simulation configurations obtained from umbrella sampling and the error bars show the standard deviation of each measurement.

Section S9 Correlations between bilayer contacts and LJ interactions

Figure S8 shows linear correlations between the Lennard-Jones (LJ) interactions and the number of NP-bilayer contacts for all three one-phase bilayers using the data from Figure 3 of the main text and Figure S12 below. These data confirm that the LJ interactions can be attributed primarily to additional NP-bilayer contacts.

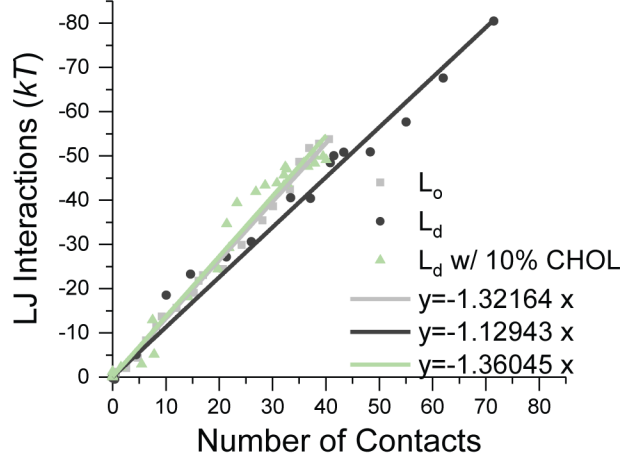


Figure S8: Linear correlation between LJ interactions and the number of NP-lipid head group contacts for the one-phase L_d bilayer, one-phase the L_o bilayer, and the one-phase L_d bilayer containing 10% cholesterol.

Section S10 Calculation of local bilayer curvature

Since the calculation of the curvature free energy (Equation 1 of the main text) requires a differentiable functional form of $h(x, y)$, we transformed the discrete MARTINI PO4 bead positions into an evenly spaced, near-continuous representation using a normalized Gaussian kernel function. We first defined a 2D rectangular grid (histogram) spanning the x - y plane of the simulation box, with the center of each grid point spaced by 0.1 nm in both the x and y directions. We define the center of the j th grid point as the position \tilde{x}_j, \tilde{y}_j , the number of lipids at that grid point as $\tilde{n}_j(\tilde{x}_j, \tilde{y}_j)$, and the bilayer height at that grid point as $\tilde{h}_j(\tilde{x}_j, \tilde{y}_j)$. The latter two quantities are computed from the PO4 bead positions for each system configuration using the following equations:

$$\tilde{n}_j(\tilde{x}_j, \tilde{y}_j) = \sum_i^{\text{PO4 beads}} \frac{1}{2\pi\sigma^2} \exp\left[-\frac{(x_i - \tilde{x}_j)^2 + (y_i - \tilde{y}_j)^2}{2\sigma^2}\right] \quad (4)$$

$$\tilde{h}_j(\tilde{x}_j, \tilde{y}_j) = \frac{1}{\tilde{n}_j(\tilde{x}_j, \tilde{y}_j)} \sum_i^{\text{PO4 beads}} \frac{1}{2\pi\sigma^2} \exp\left[-\frac{(x_i - \tilde{x}_j)^2 + (y_i - \tilde{y}_j)^2}{2\sigma^2}\right] \quad (5)$$

where x_i and y_i are the positions of bead i . The width of each Gaussian is specified by the parameter $\sigma = 0.5$ nm to approximate a MARTINI bead diameter. The height is computed for each grid point for each configuration and time-averaged, then the average height used in Equation 1 of the main text is approximated as:

$$h(x, y) \approx \tilde{h}_j(\tilde{x}_j, \tilde{y}_j) \quad (6)$$

We then numerically calculate the gradient of this function twice using a centered finite difference method in two dimensions in order to evaluate the Laplacian, $\nabla^2 \tilde{h}_j(\tilde{x}_j, \tilde{y}_j)$, at each grid point. This procedure was separately performed for each leaflet of the bilayer. After producing the $h(x, y)$ data, we summed the $\tilde{h}_j(\tilde{x}_j, \tilde{y}_j)$ values over

all of the grid points (in both leaflets) and multiplied by the area per grid point, \tilde{A} , to approximate the integral in Equation 1 of the main text, or:

$$\Delta G_{\text{curve}} = \frac{1}{2} \int_A K_c [\nabla^2 h(x, y) - \nabla^2 h_0(x, y)]^2 dA \quad (7)$$

$$\approx \frac{1}{2} \sum_j^{\text{grid points}} K_c \left[\nabla^2 \tilde{h}_j(\tilde{x}_j, \tilde{y}_j) - \nabla^2 \tilde{h}_{j,0}(\tilde{x}_j, \tilde{y}_j) \right]^2 \tilde{A} \quad (8)$$

We use the same approach to determine the radius of curvature at the phase boundary. Since $H_0(x, y)$ is alternatively defined as:

$$H_0(x, y) = \frac{1}{R_1} + \frac{1}{R_2}$$

we can determine the radius of curvature of the bilayer in the y -direction as:

$$R = \frac{1}{\frac{\partial^2 h(x, y)}{\partial^2 y}}$$

To verify the validity of this approach, we generated spatial color maps where the color represents the curvature or height at a given position \tilde{x}_j, \tilde{y}_j based on the histogram. Figure S9a shows the difference in the height of the L_d bilayer relative to a system with no NP for various values of $D_{z, \text{NP}}$. The position of the NP in the $x - y$ plane is indicated by an X and values are computed using only lipids in the top bilayer leaflet. This image shows the same trends as the radial height profiles (which are computed without the Gaussian kernel) presented in Figure 4 of the main text and the expected radial symmetry is obtained. Figure S9b shows the difference in the curvature of the L_d bilayer relative to a system with no NP for various values of $D_{z, \text{NP}}$. While more error is observed in this calculation due to the calculation of two numerical derivatives, we again obtain the expected radial symmetry and observe an increase in curvature commensurate with a change in bilayer height.

Figure S10a and b show the height and curvature, respectively, of the two-phase bilayer. These plots demonstrate that the bilayer height is nearly constant in the regions corresponding to the two individual phases and agrees with the values reported in Figure S4. Similarly, the curvature is nearly 0 in the regions corresponding to the two individual phases, negative at the interface between the phase boundary and the L_d phase, and positive at the interface of the phase boundary and the L_o phase as expected based on Figure S4. Figure S10c shows the difference in the height of the two-phase bilayer relative to a system with no NP for the same values of $D_{y, \text{NP}}$ studied in Figure S7a. The position of the adsorbed NP in the $x - y$ plane is indicated by an X and values are computed using only lipids in the top bilayer leaflet. This figure shows that the change in height is most significant for $D_{y, \text{NP}} = -7$ nm, where the bilayer curvature is initially positive, smallest for $D_{y, \text{NP}} = -11$ nm, where the bilayer curvature is initially negative, and close to zero for the other positions. All changes appear largest in the vicinity of the NP, although there are changes in height far from the NP which we attribute to bilayer undulations. Figure S10d shows the difference in the curvature of the two-phase bilayer relative to a system with no NP for the same values of $D_{y, \text{NP}}$. Again, changes in curvature match expectations compared to the average height profiles and are greatest in the regions corresponding to the individual phases and at the interface of the phase boundary and the L_o phase.

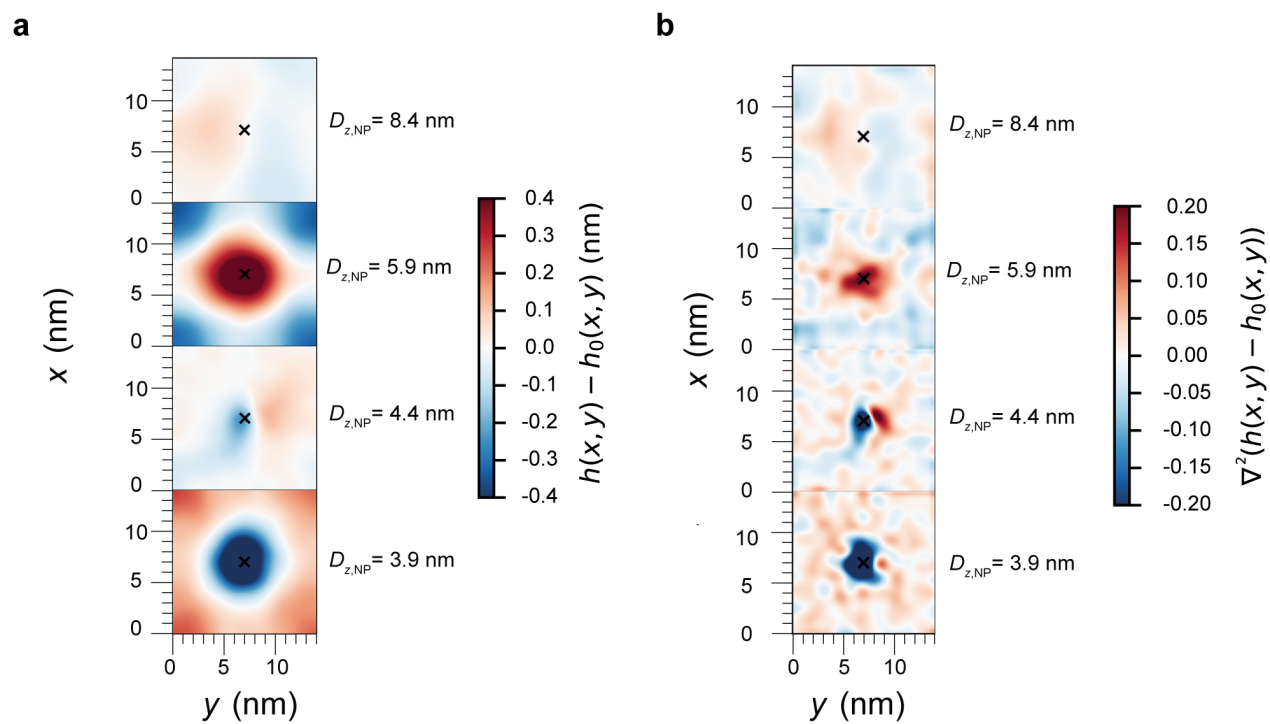


Figure S9: Bilayer height (a) and curvature (b) for a one-phase L_d bilayer at various values of $D_{z,NP}$. The X in the color maps indicates the position of the NP COM.

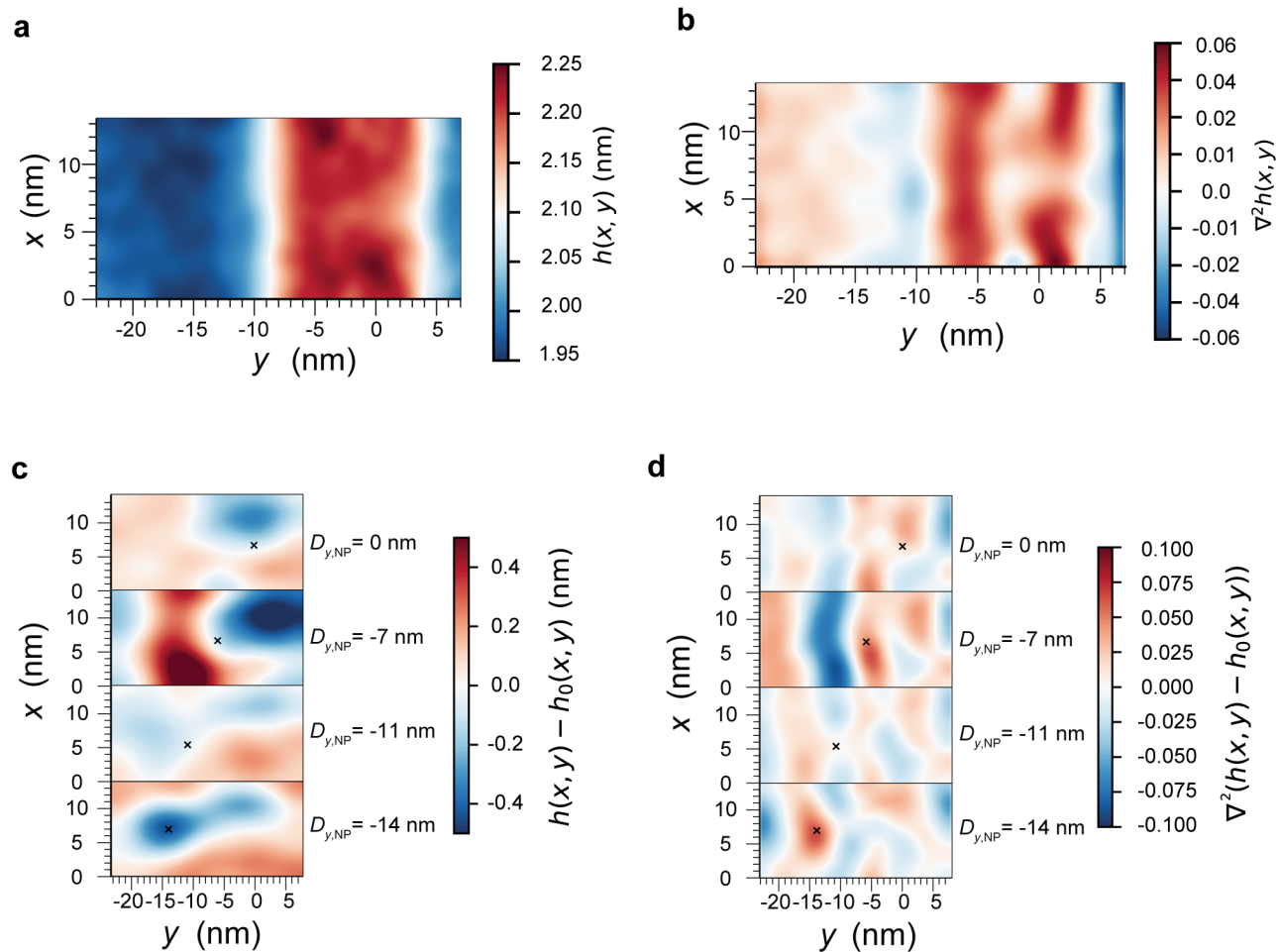


Figure S10: Bilayer height (a) and curvature (b) of a two-phase bilayer with no adsorbed NP. Difference between the bilayer height (c) and curvature (d) of a two-phase bilayer with an adsorbed NP and the same bilayer without an adsorbed NP for various values of $D_{y, \text{NP}}$. The X in the color maps indicates the position of the NP COM.

Section S11 Bilayer height near NP adsorbed to the L_o bilayer

Figure 4b of the main text presents the average height of the one-phase L_d bilayer as a function of the radial distance from the NP, $D_{r,\text{NP}}$. For comparison, Figure S11 presents the average height of the one-phase L_o bilayer as a function of $D_{r,\text{NP}}$ for various values of $D_{z,\text{NP}}$. Compared to the L_d bilayer, similar trends are observed for the L_o bilayer, but the induced curvature is in general suppressed. The curve corresponding to the PMF minimum (drawn in blue) leads to a local change in the height of the bilayer that is approximately one half the change exhibited for the L_d bilayer.

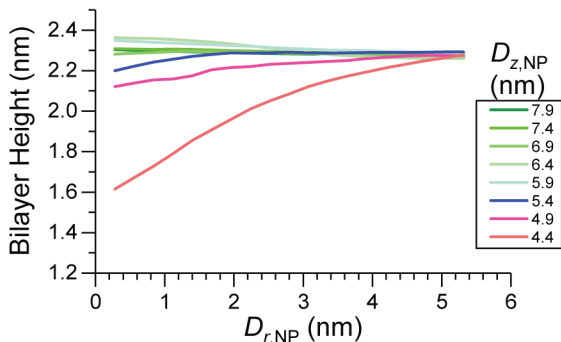


Figure S11: The average bilayer height as a function of the radial distance from the NP ($D_{r,\text{NP}}$) for the L_o bilayer. Each curve corresponds to a different value of $D_{z,\text{NP}}$. The curve corresponding to the PMF minimum in Figure 2 of the main text is shown as a bold, blue line.

Section S12 Effect of cholesterol on NP adsorption

The PMF in Figure 5b of the main text shows that the free energy change associated with moving an adsorbed NP from the L_d phase to the L_o phase of a two-phase bilayer is nearly zero, while the one-phase PMFs presented in Figure 2 of the main text suggests that the NP should preferentially adsorb to the L_d phase. However, Figure 5a of the main text shows that the composition of the L_d phase in the two-phase bilayer contains 10% CHOL after equilibration, which might explain the apparent discrepancy between these results. We thus performed additional simulations to compute the properties and NP adsorption free energy for a one-phase bilayer containing 90% DIPC and 10% CHOL. The bilayer was again prepared with the INSANE script and equilibration and umbrella sampling were performed using the same protocol previously used for the other one-phase bilayers. We then characterized the bilayer phase by calculating the P_2 order parameter as discussed in Section S5. Table S3 shows that the calculated value (0.23) is nearly the same as the value calculated for the L_d phase with no cholesterol (0.22), indicating the bilayer is indeed in the L_d phase.

We next performed umbrella sampling simulations to compute the PMF for NP adsorption to the one-phase L_d bilayer with 10% CHOL following the same procedure as the other one-phase bilayers. Figure S12a shows the PMF as a function of $D_{z,\text{NP}}$ for all three one-phase bilayers. The PMF for the L_d bilayer with 10% CHOL is similar to the PMF for the L_d bilayer with no cholesterol, but the adsorption free energy (*i.e.*, the PMF minimum) is only $-37.8 \pm 1.6 kT$, compared to $-46.1 \pm 1.1 kT$ for the L_d bilayer with no cholesterol (Figure 2 of the main text). Moreover, the adsorption free energy is similar to the value of $-38.1 \pm 1.0 kT$ reported for adsorption to the one-phase L_o bilayer. This result is thus consistent with the near-zero difference in the free energy between the L_d and L_o phases observed in Figure 5b of the main text. The agreement between the one-phase adsorption PMFs and the two-phase PMF further indicates that the two-phase bilayer correctly samples bulk phase behavior, albeit over a limited range of the reaction coordinate.

Figure S12b shows the change in the bilayer height for all three one-phase bilayers to compare the deformation induced by NP adsorption in analogy to Figure 4b of the main text. As expected, the behavior of the L_d bilayer with

10% CHOL is similar to that of the L_d bilayer with no cholesterol, indicating that the bending modulus is similar between these two bilayers. Conversely, the L_o exhibits a much smaller curvature deformation due to its larger bending modulus. Figure S12c similarly compares the Lennard-Jones (LJ) interactions and number of NP-bilayer contacts between all three one-phase bilayers in analogy to Figure 3 of the main text, with vertical dashed lines indicating the values of $D_{z, NP}$ corresponding to PMF minima. The LJ interactions at the PMF minimum are $-49.4 kT$ for the L_d bilayer with 10% CHOL compared to $-57.9 kT$ for the L_d bilayer with no cholesterol. This $8.3 kT$ difference is similar to the $8.5 kT$ difference in the adsorption free energies between these two phases. Finally, Figure S12d compares the curvature free energy of all three one-phase bilayers in analogy to Figure 4a of the main text. The curvature free energy of the L_d bilayer with 10% CHOL is calculated assuming the same bending modulus as the L_d bilayer with no cholesterol, leading to a very similar curvature free energy.

Together, these data suggest that NP adsorption to a L_d bilayer with 10% CHOL is weaker than adsorption to a L_d bilayer with no cholesterol due to weaker LJ interactions. The additional cholesterol does not affect the curvature response of the bilayer or corresponding curvature free energy. This result resolves the seeming discrepancy between the one-phase PMFs in Figure 2 of the main text and the two-phase PMF in Figure 5b of the main text by showing that the cholesterol content in the L_d phase of the two-phase bilayer affects the NP adsorption free energy.

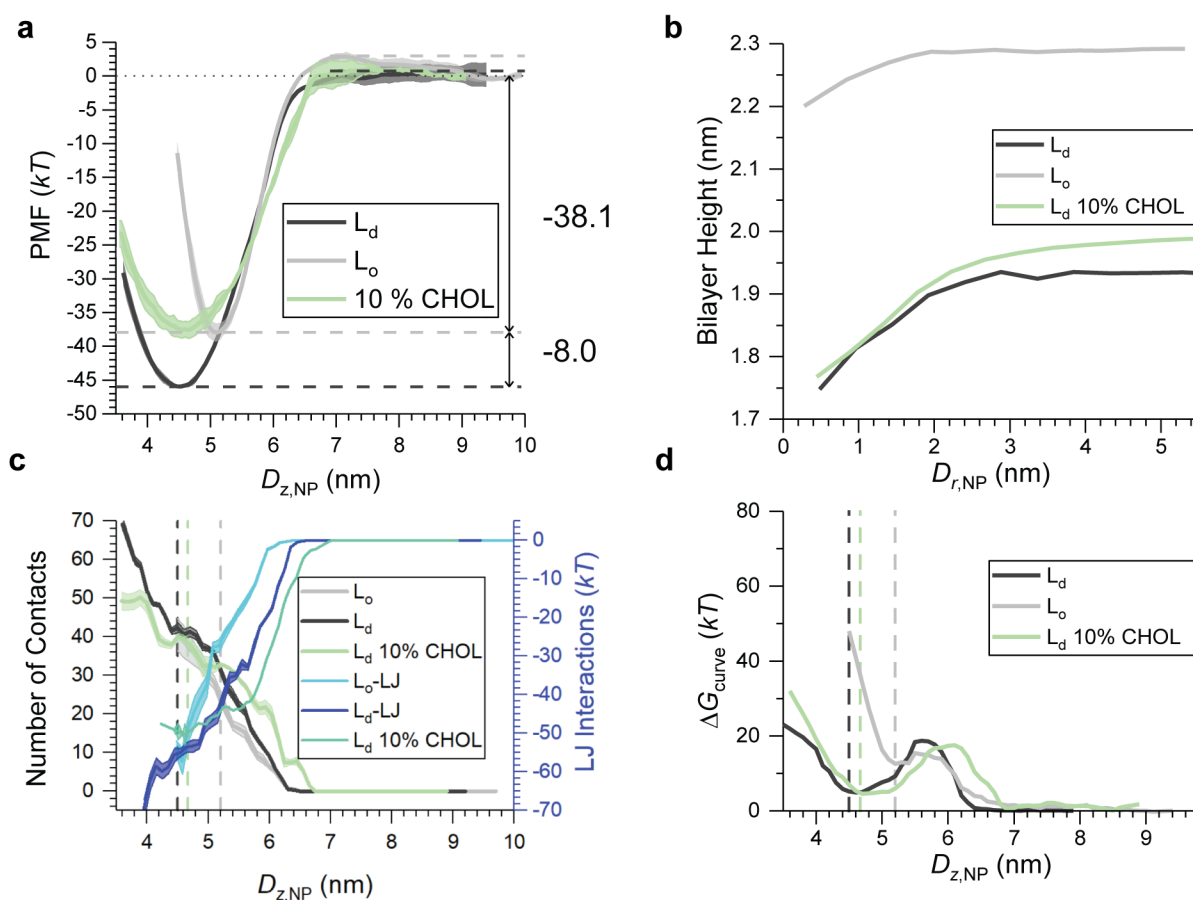


Figure S12: Analysis of the L_d bilayer with 10% cholesterol, in comparison to the data reported for the one-phase L_d and L_o bilayers reported in the main text. **a)** Comparison of PMFs for NP adsorption to all three bilayers as a function of $D_{z, NP}$. **b)** Comparison of the bilayer height as a function of $D_{r, NP}$ for all three bilayers. The height is reported for the values of $D_{z, NP}$ corresponding to the PMF minima from **a**. **c)** The LJ interactions and the number of NP-lipid head group contacts as a function of $D_{z, NP}$. **d)** The change in the curvature free energy, ΔG_{curve} , as a function of $D_{z, NP}$.

References

- [1] Z. Wu, Q. Cui and A. Yethiraj, *Journal of Chemical Theory and Computation*, 2011, **7**, 3793–3802.
- [2] S. O. Yesylevskyy, L. V. Schäfer, D. Sengupta, S. J. Marrink, L. V. Schaefer, D. Sengupta and S. J. Marrink, *PLoS computational biology*, 2010, **6**, 1–17.
- [3] S. J. Marrink, H. J. Risselada, S. Yefimov, D. P. Tieleman and A. H. de Vries, *The Journal of Physical Chemistry B*, 2007, **111**, 7812–7824.
- [4] W. Ding, M. Palaiokostas, W. Wang and M. Orsi, *The Journal of Physical Chemistry B*, 2015, **119**, 15263–15274.
- [5] E. S. Melby, A. C. Mensch, S. E. Lohse, D. Hu, G. Orr, C. J. Murphy, R. J. Hamers and J. A. Pedersen, *Environmental Science: Nano*, 2016, **3**, 45–55.
- [6] M. Tosi and F. Fumi, *Journal of Physics and Chemistry of Solids*, 1964, **25**, 45 – 52.
- [7] Z. Wu, Q. Cui and A. Yethiraj, *The Journal of Physical Chemistry B*, 2013, **117**, 12145–12156.
- [8] S. J. Marrink, A. H. de Vries and A. E. Mark, *The Journal of Physical Chemistry B*, 2004, **108**, 750–760.
- [9] G. W. Feigenson, *Biochimica et Biophysica Acta (BBA) - Biomembranes*, 2009, **1788**, 47–52.
- [10] R. S. Davis, P. B. Sunil Kumar, M. M. Sperotto and M. Laradji, *The Journal of Physical Chemistry B*, 2013, **117**, 4072–4080.
- [11] T. A. Wassenaar, H. I. Ingólfsson, R. A. Böckmann, D. P. Tieleman and S. J. Marrink, *Journal of Chemical Theory and Computation*, 2015, **11**, 2144–2155.
- [12] H. J. Risselada and S. J. Marrink, *Proceedings of the National Academy of Sciences*, 2008, **105**, 17367–17372.
- [13] A. M. Smondyrev and M. L. Berkowitz, *Biophysical Journal*, 1999, **77**, 2075 – 2089.
- [14] J. F. Nagle and S. Tristram-Nagle, *Biochimica et Biophysica Acta (BBA)-Reviews on Biomembranes*, 2000, **1469**, 159–195.
- [15] J. S. Hub, B. L. de Groot and D. van der Spoel, *Journal of Chemical Theory and Computation*, 2010, **6**, 3713–3720.